

## PROFILES OF Ly $\alpha$ EMISSION LINES OF THE EMITTERS AT $z = 3.1$

T. YAMADA<sup>1</sup>, Y. MATSUDA<sup>2</sup>, K. KUSAI<sup>3</sup>, T. HAYASHINO<sup>3</sup>, N. MORIMOTO<sup>1</sup>, AND M. UMEMURA<sup>4</sup>

<sup>1</sup> Astronomical Institute, Tohoku University, Aramaki, Aoba-ku, Sendai, Miyagi 980-8578, Japan; [yamada@astr.tohoku.ac.jp](mailto:yamada@astr.tohoku.ac.jp)

<sup>2</sup> Department of Physics, Durham University, South Road, Durham DH1 3LE, UK

<sup>3</sup> Research Center for Neutrino Science, Graduate School of Science, Tohoku University, Sendai 980-8578, Japan

<sup>4</sup> Center for Computational Physics, University of Tsukuba, Tsukuba, Ibaraki 305, Japan

Received 2011 November 22; accepted 2012 March 14; published 2012 May 1

### ABSTRACT

We present the results of the observations of the Ly $\alpha$  line profiles of 91 emission-line galaxies at  $z = 3.1$  with a spectral resolution of  $\lambda/\delta\lambda(\text{FWHM}) \approx 1700$  or  $180 \text{ km s}^{-1}$ . A significant fraction of  $\sim 50\%$  of the observed objects show the characteristic double peaks in their Ly $\alpha$  profile. The red peak is much stronger than the blue one for most of the cases. The red peaks themselves also show weak but significant asymmetry and their widths are correlated with the velocity separation of the red and the blue peaks. This implies that the peaks are not isolated multiple components with different velocities but parts of a single line that are modified by the absorption and/or scattering by the associated neutral hydrogen gas. The characteristic profile can be naturally explained by scattering in the expanding shell of the neutral hydrogen surrounding the Ly $\alpha$  emitting region while the attenuation by the intergalactic medium should also be considered. Our results suggest that the star formation in these Ly $\alpha$  emitters are dominated by young burst-like events that produce the intrinsic Ly $\alpha$  emission as well as the gas outflow.

**Key words:** galaxies: evolution – galaxies: formation – galaxies: high-redshift – galaxies: kinematics and dynamics – galaxies: star formation

### 1. INTRODUCTION

A large number of Ly $\alpha$  emitters at a high redshift have been detected in a sensitive search using narrowband filters (e.g., Hu & McMahon 1996; Steidel et al. 2000; Rhoads & Malhotra 2001; Rhoads et al. 2003; Kodaira et al. 2003; Palunas et al. 2004; Hayashino et al. 2004; Matsuda et al. 2004; Taniguchi et al. 2005; Gronwall et al. 2007; Iye et al. 2006; Ouchi et al. 2008). From the photometric study, they are generally considered to be young star-forming objects and found to be widely distributed in their luminosity, size, and equivalent width (e.g., Gawiser et al. 2007; Finkelstein et al. 2007).

While Ly $\alpha$  emission is one of the fundamental tools to study galaxy formation at a high redshift, it is, however, still difficult to understand what the dominant origins of Ly $\alpha$  emission are, and how Ly $\alpha$  photons escape from the galaxy. Resonance scattering and extinction by neutral hydrogen or dust in galaxies may easily modify the observed flux and line profile. There are at least three different physical origins of the Ly $\alpha$  lines from high-redshift, star-forming galaxies: photoionization by hot massive stars, cooling radiation from gas heated either by the shock during the gravitational collapse or by the shock due to the gas outflow driven by the thermal energy of frequent supernovae or active galactic nuclei (AGNs). The Ly $\alpha$  photons produced by any of these processes are affected by neutral hydrogen gas mixed with or surrounding the emission-line regions. Hayes et al. (2010) reported that the statistical average of the Ly $\alpha$  escape fraction from a sample of the star-forming galaxies at redshift  $z \sim 2$  is only  $\sim 5\%$ .

It is important to study their spectroscopic properties, especially their line profiles, to learn how the lines are produced and modified. If the Ly $\alpha$  emission is largely reprocessed by neutral gas with a large bulk motion, we may observe signatures in their line profiles. For example, Dijkstra et al. (2006a, 2006b) studied the expected Ly $\alpha$  profile of optically thick, spherically symmetric collapsing gas clouds. The expected profiles are generally blueshifted and show a double-peaked profile possibly

dominated by the blue peak due to the combination of the in-falling gas motion and line radiation transfer effects. On the other hand, Verhamme et al. (2006, 2008) modeled the line profiles expected for the expanding neutral hydrogen shell. Although the expected profiles are also double-peaked, in many cases they are redshifted and the red peak appears stronger due to the scattered components behind the original Ly $\alpha$  emission-line region in our line of sight. It is, however, not easy to discriminate these two cases from the observation of the individual Ly $\alpha$  line itself if we do not know the systemic velocity.

It is known that high-redshift, star-forming galaxies typically show gas outflow from sources. Pettini et al. (2001) and Shapley et al. (2003) compared the redshifts of the interstellar absorption line with the rest-frame optical emission lines that are nearly at the systemic velocity of the photoionized region and found that interstellar absorption gas is generally blueshifted for typically  $200 \text{ km s}^{-1}$ , indicating that the outflow gas motion is common among the Lyman break galaxies. Ly $\alpha$  lines in these objects also show P Cyg-type profiles, namely, a narrow emission line with a blueshifted absorption line. Verhamme et al. (2008) applied their models to the Ly $\alpha$  line profile of the Lyman break galaxies and found that they can be explained by scattering in the simple expanding shell models. Steidel et al. (2010) also showed that the cool gas around  $z = 2\text{--}3$  Lyman break galaxies typically exhibit outward motion.

On the other hand, the models of cold accretion (Dekel et al. 2009; Goerdt et al. 2010) also suggest that the observed luminosity, surface brightness, and size distributions of Ly $\alpha$  emitters, especially for the extended Ly $\alpha$  blobs (Steidel et al. 2000; Matsuda et al. 2004), can be explained by the gas heated by the collisional excitation in the cold gas stream. Hayes et al. (2011) also recently reported the detection of polarization in the Ly $\alpha$  emission in a giant Ly $\alpha$  blob, which indicates that the extended Ly $\alpha$  photons are indeed re-scattered by neutral hydrogen.

Spectroscopic observations to study the line profiles of Ly $\alpha$  emitters are essential to discriminate these cases, although

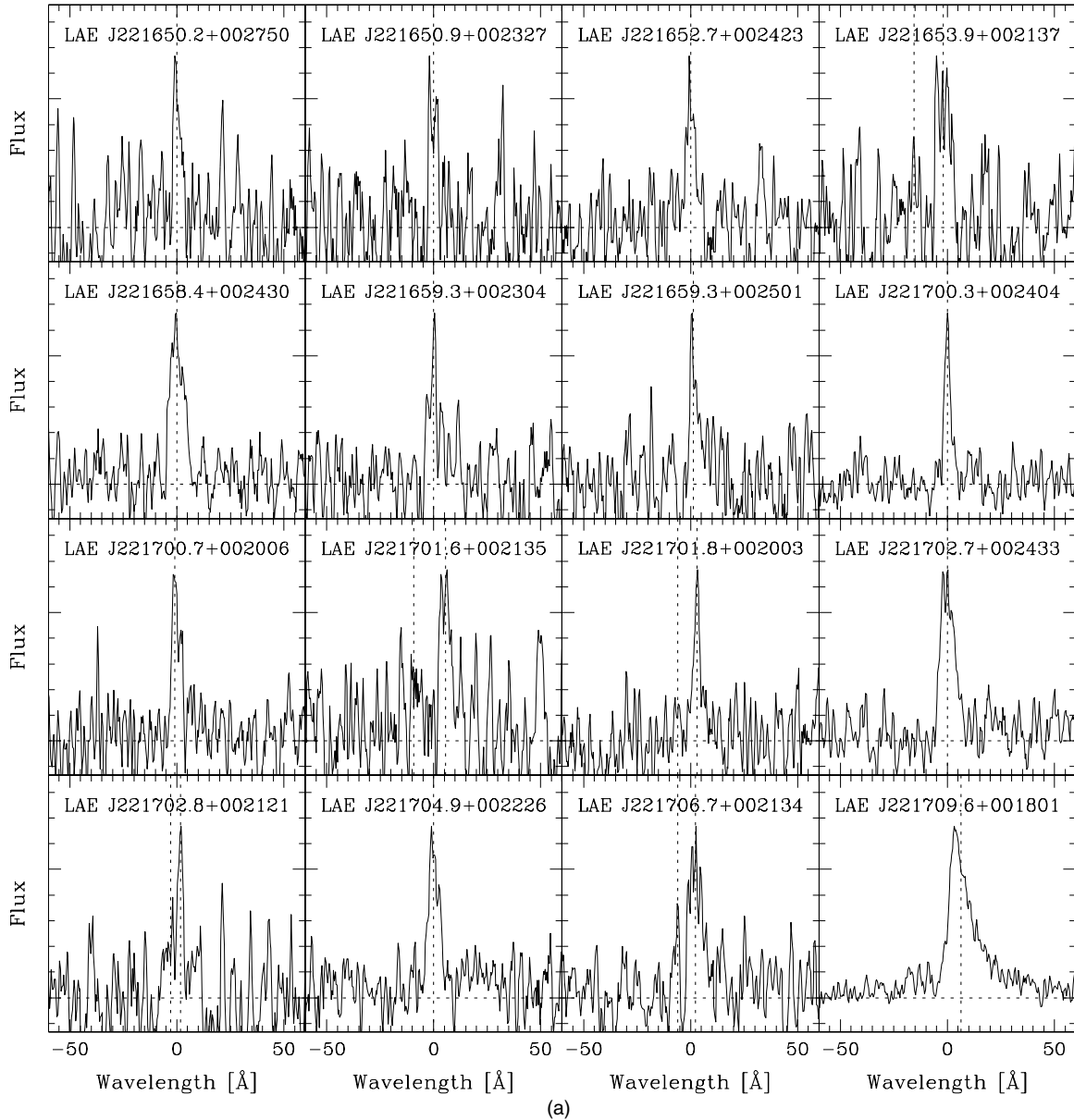


**Figure 1.**  $\text{Ly}\alpha$  profile of the 91 *NB497*-selected emission-line objects at  $z = 3.1$  in SSA22-Sb1. The plot is centered at the central wavelength of the single Gaussian fitting. The vertical dotted lines show the center of the main and the significant secondary peaks in the multi-component Gaussian fitting.

only a small sample of spectroscopy with enough high spectral resolution is available so far. Matsuda et al. (2006) studied the line profiles of the extended  $\text{Ly}\alpha$  emitters, or  $\text{Ly}\alpha$  blobs, as well as more “ordinary”  $\text{Ly}\alpha$  emitters, and found that the  $\text{Ly}\alpha$  lines of the blobs have more structure and the whole velocity width is positively correlated with their size.

In this paper, we present the results of our new spectroscopic observations for the 91  $\text{Ly}\alpha$  emitters to show their  $\text{Ly}\alpha$  line profiles. The photometric data for the sample selection are similar to Matsuda et al. (2006), but the number of spectra for normal  $\text{Ly}\alpha$  emitters is significantly higher. We describe our observations and data reduction in Section 2, the observed line profiles in Section 3, and the discussion in Section 4.

## 2. OBSERVATIONS AND DATA REDUCTION

The sample of  $\text{Ly}\alpha$  emitters (LAE) is selected based on the same data presented in Hayashino et al. (2004) and Yamada et al. (2012) at the field of SSA22-Sb1 where one of the largest

overdensities of Lyman break galaxies as well as  $\text{Ly}\alpha$  emitters at  $z = 3.1$  is known to exist (Steidel et al. 1998, 2000). The selection criteria for the emitters are, however, slightly modified to include objects with relatively low equivalent width. We also did not use the  $B - V$  color criteria, which was needed to make the very robust imaging sample of  $\text{Ly}\alpha$  emitters to exclude contamination by the foreground objects. We here applied only the following criteria:

$$BV - NB497 > 0.5 \quad \text{and} \quad NB497 < 25.5,$$

or

$$BV - NB497 > 1.0 \quad \text{and} \quad NB497 < 26.0,$$

where  $BV$  is the effectively averaged AB magnitude of the  $B$  and the  $V$  band and  $NB497$  represents the AB magnitude in the *NB497* narrowband filter (Hayashino et al. 2004).

The observations of the  $\text{Ly}\alpha$  profiles of the emitters are done by the Faint Object Camera And Spectrograph (FOCAS)

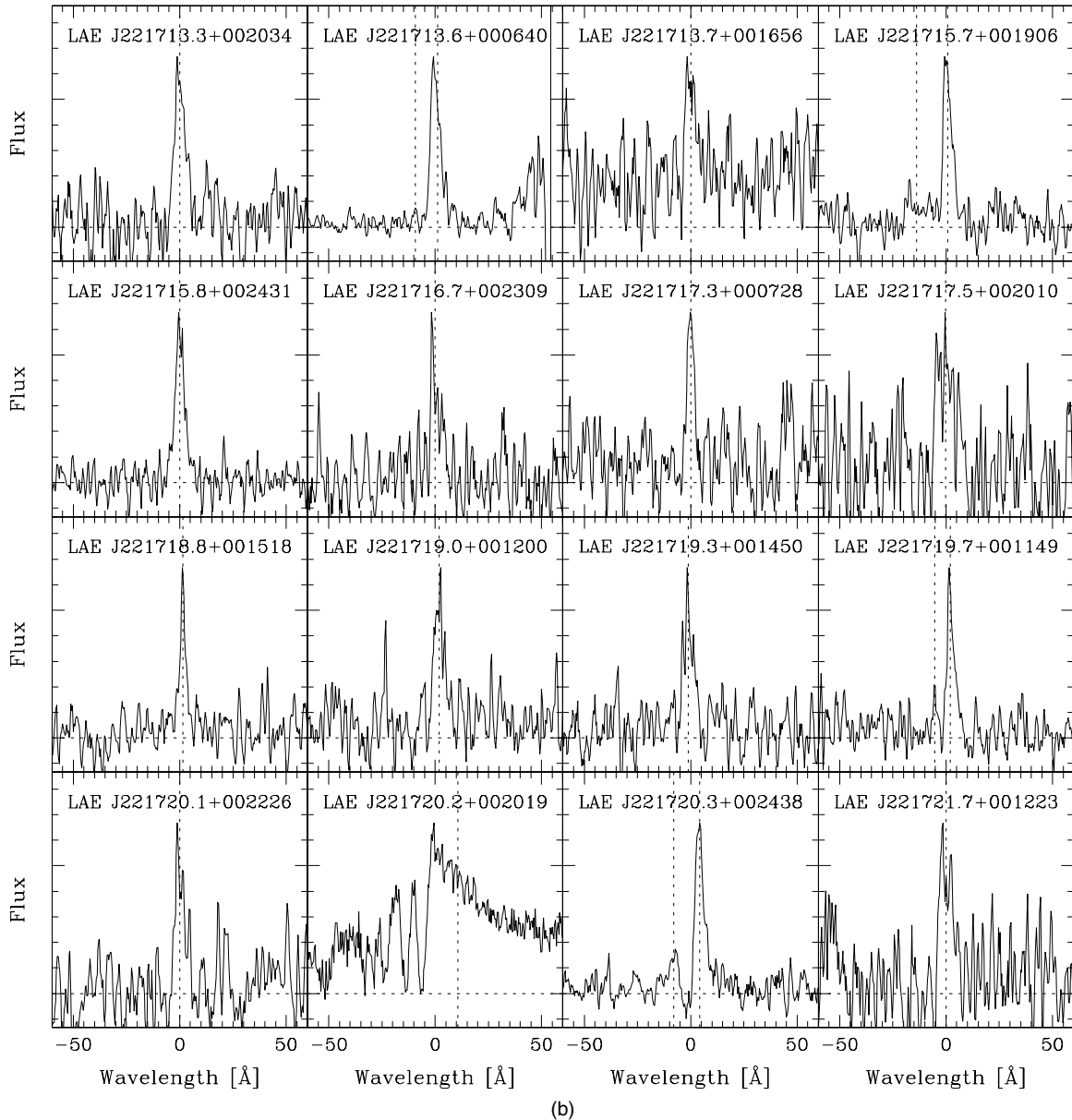


Figure 1. (Continued)

equipped with the Subaru 8.2 m telescope in 2004 July to 2005 August. The Volume-Phase Holographic grating 600\_450 was used to obtain the spectral dispersion of  $0.37 \text{ \AA pixel}^{-1}$ . Using slits with a width of 1 arcsec and spectral resolution,  $\lambda/\delta\lambda \approx 1700$  was achieved as measured from the widths of the arc lines. In order to observe as many targets as we can in one exposure, we used the custom-made intermediate-band filter with  $\delta\lambda \sim 200 \text{ \AA}$  to limit the spectral length of the detectors. By this method, we obtain the range of the spectra only around the emission lines, but the spectral resolution is high enough to clearly discriminate the [O II] 3727  $\text{\AA}$  doublet, which is the only significant contaminant, from the  $z = 3.1$  Ly $\alpha$  lines. The data were reduced in the standard manner using IRAF. The accuracy of the wavelength calibration is higher than  $0.2 \text{ \AA}$ . The one-dimensional spectra are then extracted by averaging the three spatial pixels, each  $0''.2$ . We also smoothed the spectra by 3 pixels in the dispersion direction.

As a result, we obtained Ly $\alpha$  emission-line spectra for the 91 objects. The sample contains the 12 objects classified as Ly $\alpha$  blobs by Matsuda et al. (2004) whose isophotal area above

the surface brightness of  $\approx 7 \times 10^{-17} \text{ erg s}^{-1} \text{ cm}^{-2} \text{ arcsec}^{-2}$  is larger than  $16 \text{ arcsec}^2$  or  $900 \text{ kpc}^2$  at  $z = 3.1$ . Matsuda et al. (2004, 2006) showed that the photometric or the spectroscopic properties of the Ly $\alpha$  blobs are not quite discriminated from other objects but rather continuously distributed in the whole sample of the emitters.

As described in Matsuda et al. (2005) and Matsuda et al. (2006), the sample selected by the criteria in Hayashino et al. (2004) is almost free of contamination ( $< 1\%$ ). For the objects with a lower equivalent width (i.e.,  $0.5 < BV - NB497 < 1.2$ ), the fraction of the [O II] emitter at  $z = 0.33$  increases, as expected, but is still less than  $\sim 5\%$ . We identified a total of 91 spectroscopic Ly $\alpha$  emitters in the 11 masks located in the SSA22-Sb1 field.

### 3. OBSERVED LINE PROFILES

Figures 1(a)–(f) show the observed Ly $\alpha$  spectrum for all 91 objects. Two of them (LAE J221709.6+001801 and

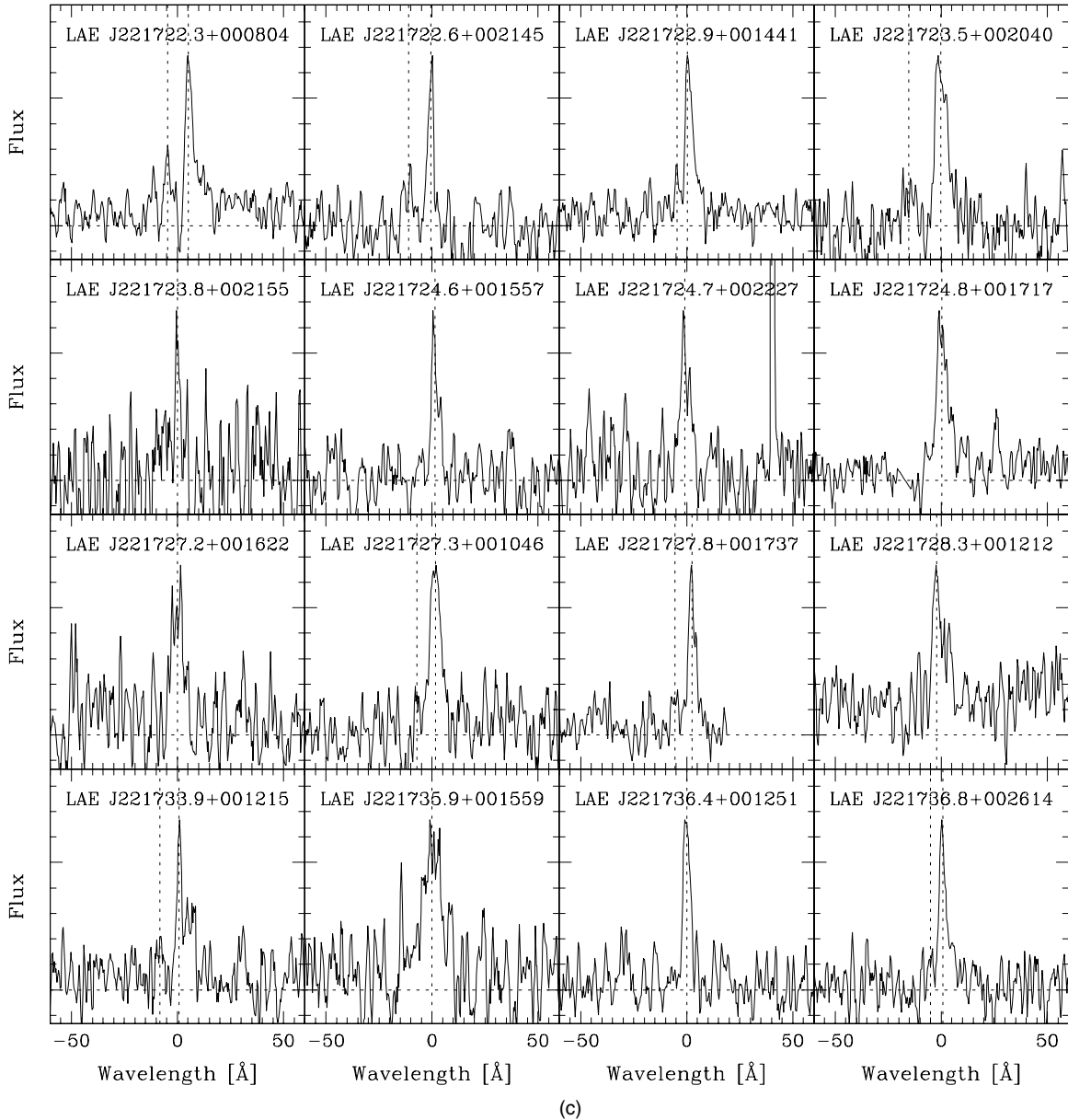


Figure 1. (Continued)

LAE J221720.2+002019) clearly show a very large line width ( $\gtrsim 1000 \text{ km s}^{-1}$ ) and possibly host AGNs. Table 1 summarizes their observed properties.

In Figure 1, we first notice that many of the objects show characteristic profiles, namely, the double-peaked spectra with a strong, asymmetrical red peak and a much weaker blue peak. While the most conspicuous cases are the objects LAE J221720.3+002438, LAE J221745.3+002006, and LAE J221759.2+002254 (LAB28 in Matsuda et al. 2004), many other cases can be recognized in Figure 1. As a large fraction of the observed Ly $\alpha$  spectra shows similar profiles, it may represent the common physical properties of the emitters.

We therefore tried to characterize the profile and to evaluate the fraction of the objects with similar profiles among those observed in a more objective way. We first fitted the visually isolated peaks in each spectrum with the Gaussian profiles. These procedures are rather formal ones but useful in the following discussions. Figures 2 and 3 show the example of the fitting for two objects with a high and moderate

signal-to-noise ratio (S/N), respectively. Figures 2(a) and 3(a) are for the multiple Gaussian fittings. The green lines show each component and the blue ones the total. The red dashed lines in the figures show the noise level measured at the same wavelength by using the blank part of the slits. Bottom panels show the residual. On the other hand, Figures 2(b) and 3(b) show examples of the single Gaussian fitting similar to those tried in Matsuda et al. (2006). For the objects with multiple peaks, the data points between the peaks are not used for the fitting (thin crosses in Figures 2(b) and 3(b)). The center of the wavelength in each panel in Figure 1 is the central wavelength of the single-component Gaussian fitting. The central wavelengths of the primary red and secondary blue peaks (for the objects with this feature) as well as that of the single-component fitting (for all the objects) are also presented in Table 1.

Of the 89 objects, except for the 2 broad-line AGNs, 50 objects have the visually identified strong blue and weak red peaks. Four other objects (221728.3+001212, 221740.3+001129, 221740.9+001125, and 221812.5+001433)

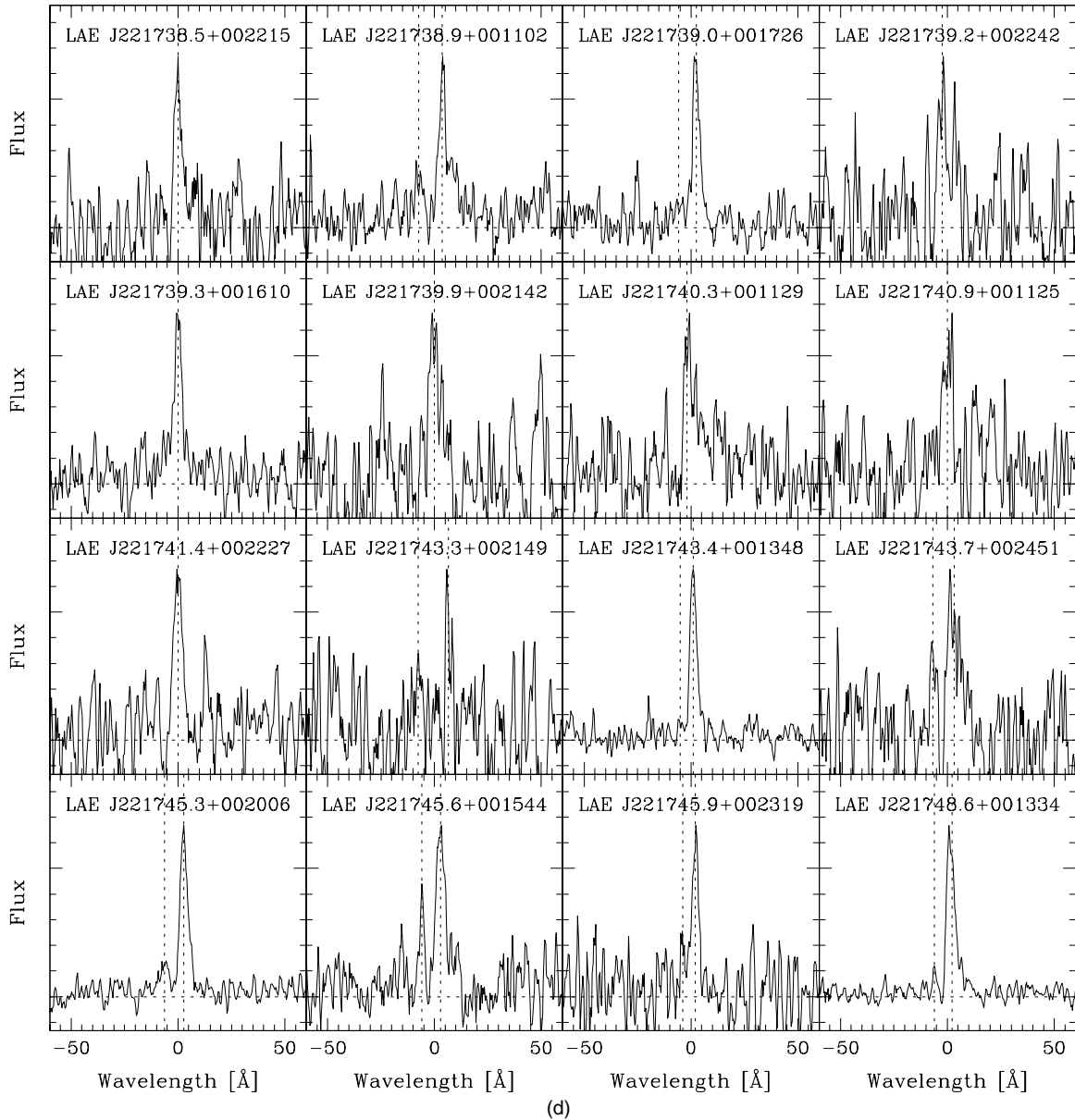


Figure 1. (Continued)

do not show the weak blue peaks but have notable components of the red of the strongest peak. Three of these four objects, 221728.3+001212, and the closely located objects 221740.3+001129 and 221740.9+001125, are associated with the Ly $\alpha$  blobs LAB33 and LAB7 in Matsuda et al. (2004), respectively.

For the 50 candidates of the “strong red and weak blue” profiles, we then evaluated the significance of the weak peaks relative to the noise level. We evaluated the rms noise in the blank-sky spectra (the red dashed lines in Figures 2 and 3 for the example) at the line core ( $\pm 2\sigma_\lambda$  of the Gaussian) and then selected only the objects with weak peaks that were more significant than the  $3\sigma$  level as the final sample of the “strong red and weak blue” profiles. For the cases between  $3\sigma$  and  $4\sigma$ , we further visually checked the spectra and rejected a few cases. After all, 39 of the 89 objects (44%) show the significant characteristic profile. The wavelength of the primary and the secondary peaks are shown by the vertical dotted lines in Figure 1. This is a large fraction, which implies that the “strong

red and weak blue” profile is a common characteristic of the observed Ly $\alpha$  emitters. This fraction should even be considered as the lower limit because it is more difficult to significantly detect the secondary weaker peaks if the objects are faint or their emission lines are weak. Indeed, if we limit the objects with  $NB497 < 25$  and further with  $BV - NB497 > 1.0$ , the fraction is even larger, 53% and 55%, respectively. Table 2 summarizes the number of objects with this characteristic profile. We also listed the wavelength of the secondary component for five marginal objects whose blue peaks were visually identified but not found to be significant.

While it is difficult to tell whether the peaks are multiple emission lines with different central velocities or a single line modified by absorption and/or scattering by neutral gas in the vicinity only from such formal fitting procedures as shown in Figures 2 and 3, the latter interpretation is plausible because such a large fraction of the sample always shows a much stronger peak at the long wavelength. We confirm this further by the following two different methods.



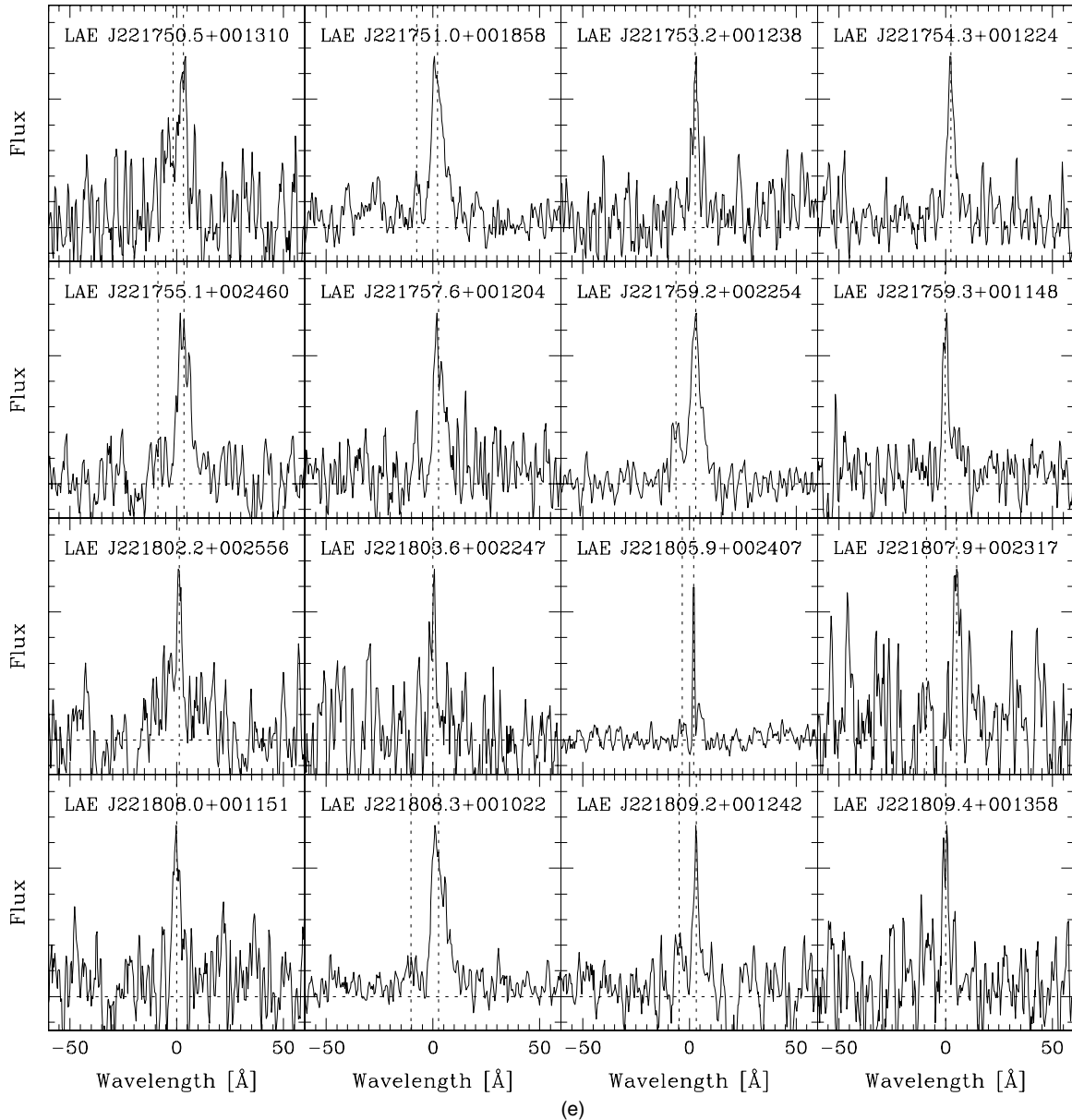


Figure 1. (Continued)

First, we investigated the asymmetry of the strongest peaks of the sample. We identify the pixel with the largest flux and obtained the ratio of the flux integrated over  $4.5 \text{ \AA}$  (about 1.5 times the spectral resolution) toward a longer wavelength to those toward a shorter wavelength. Figure 4 shows the result for the objects with  $NB497 < 25.0$  and  $BV - NB407 > 1.0$ , avoiding the objects with relatively low S/N. The symmetry index (ratio) of those with the characteristic “strong red and weak blue” profile is strongly concentrated around 0.5 while those of the other objects are distributed around the unity (the median is 0.83) with an rms scatter of  $\sim 0.25$ . Twelve objects with the characteristic profile have the value below 0.6 and they indeed show the conspicuous “strong red and weak blue” profiles. We applied the Kolmogorov–Smirnov test to the symmetry distribution of the objects with and without the characteristic profile and the probability that they are drawn from the same population is 7%. We also changed the magnitude or color range as well as the wavelength region for the index and found that the trend is always seen.

Next, for those objects with the characteristic profile, we compared the observed width of the stronger red peak and the separation of the peaks obtained in the formal Gaussian fitting. Figure 5 shows the result; a clear correlation between these two quantities is seen. This strongly supports the theory that the two peaks are indeed parts of a single feature. If they were multiple different components, the trend as seen in Figure 5 would not be necessary to be observed. Figure 6 shows the distribution of the observed FWHM for the most prominent peak of each object. Those with the characteristic profile tend to show the smaller values.

## 4. DISCUSSIONS

### 4.1. Characteristic $\text{Ly}\alpha$ Line Profile

We found that a large fraction,  $>40\%$  of the observed  $\text{Ly}\alpha$  emitters in the SSA22-Sb1 field, have a characteristic double-peaked line profile with a strong red peak and a much weaker blue peak. What does this characteristic  $\text{Ly}\alpha$  profile

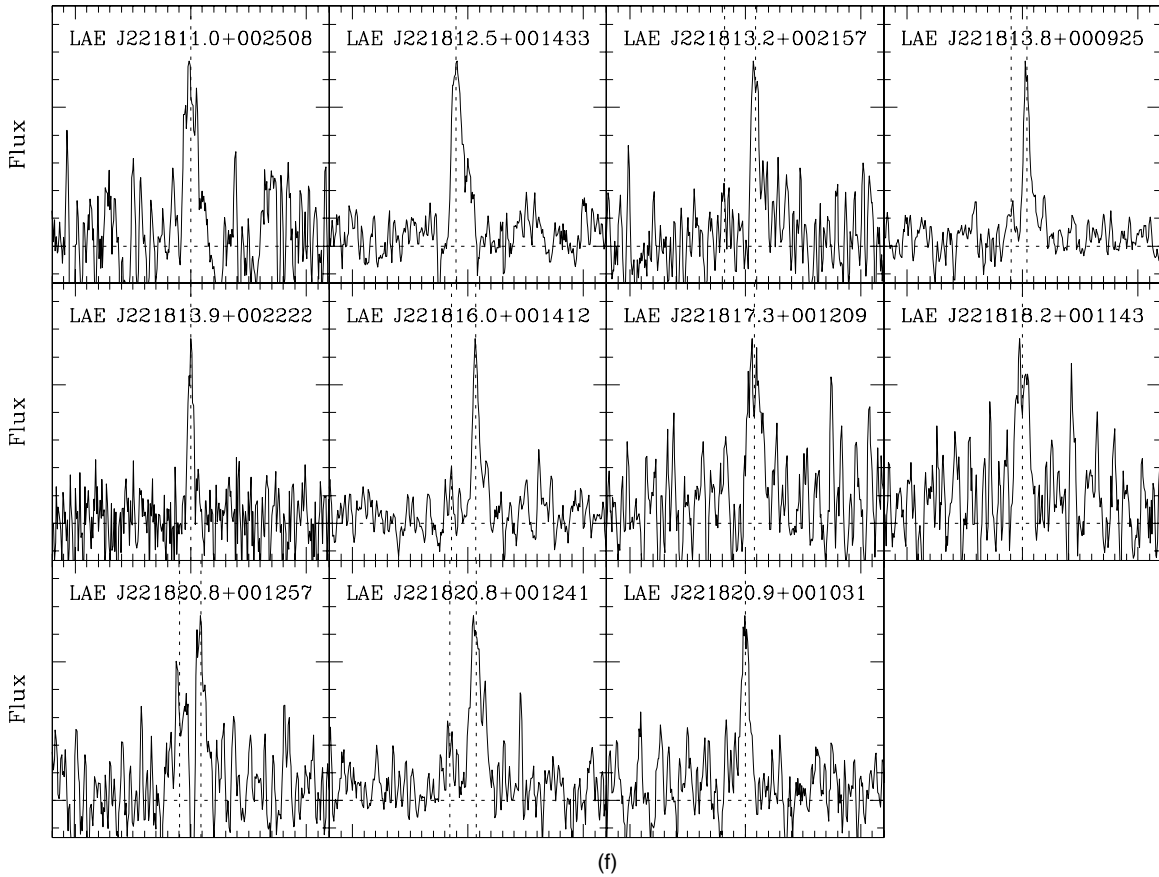


Figure 1. (Continued)

mean? The double-peaked profiles can be a single source absorbed or scattered by neutral hydrogen gas or multiple components of the ionized gas with different velocities. The multiple-component cases are not favored, however, as the observed lines show asymmetry and there is a correlation between the peak separation and the line width as described in the previous section.

$\text{Ly}\alpha$  line profile emission is affected by the intergalactic medium (IGM) in the line of sight of the object (Dijkstra et al. 2007; Laursen et al. 2011). At  $z \sim 3$ , the mean transmission of the photon at a wavelength just shorter than  $\text{Ly}\alpha$  due to the absorption by the foreground intergalactic  $\text{Ly}\alpha$  clouds is  $\sim 0.7$  (Madau & Shull 1996). Due to the fluctuation by the large-scale structure, the absorption varies by the line of sight toward the sources. Laursen et al. (2011) recently examined how the line profile of the  $\text{Ly}\alpha$  emitter at  $z = 2.5\text{--}6.5$  is affected by IGM absorption. The case for  $z = 3.5$  (their Figure 7) indeed predicts the double-peaked  $\text{Ly}\alpha$  line profile with a stronger red component. The red and blue peak-strength difference is more conspicuous for the smaller objects. As the size of the emitter becomes larger, the two peaks show comparable strength on average although the distribution of the IGM optical depth can produce a variation of profiles. This prediction may be compared with our observed results. For those objects identified to have the characteristic profile, most of them show a large flux difference between the red and blue peaks and there are few objects with comparable strength (Figure 1). The formal single-component Gaussian fitting shows that more than 50% of the line flux is absorbed for typical cases (e.g., Figure 2(b), Figure 3(b)). It seems difficult to explain the current results

only by IGM absorption in this sense. However, note that the emitters observed here are located in a dense environment and the IGM absorption is much larger than the average. We revisit this possibility in Section 4.4.

We then consider the cases where the profiles show the intrinsic properties of the  $\text{Ly}\alpha$  emitters, namely, the effects by the gas associated with them. Scattering in the infalling partially ionized emission-line gas (Dijkstra et al. 2006a) as well as scattering in the expanding shell-like outflowing gas (Verhamme et al. 2006, 2008) can modify the line profile. For the case of the spherically symmetric infalling gas model, Dijkstra et al. (2006a) argued that the entire line profile shows a strong blue symmetry and the blue peaks are observed to be stronger than the red peaks. As the red peaks are much stronger than the blue peak for most of the cases studied here, the other interpretation, namely, the expanding shell model is more favored. For the spherically symmetrical expanding shell model (Verhamme et al. 2006) surrounding the  $\text{Ly}\alpha$  source, the  $\text{Ly}\alpha$  line is shifted redward from the systemic velocity and also shows a strong red asymmetry. Indeed, some model profiles shown in Verhamme et al. (2006, their Figure 15) as well as in Verhamme et al. (2008) seem quite similar with the characteristic “strong red and weak blue” profiles discussed here. Recently, McLinden et al. (2011) reported that a strong [O III] 5007 Å emission line was detected for an  $\text{Ly}\alpha$  emitter at  $z = 3.1$ , which shows the similar double-peaked  $\text{Ly}\alpha$  profile. Interestingly, the [O III] line is located in the middle of the two  $\text{Ly}\alpha$  peaks, which implies that the systemic velocity of the galaxy is indeed in the middle of the two  $\text{Ly}\alpha$  peaks. Thus, the expanding shell by Verhamme et al. (2008) is favored to understand the observed line profiles.

**Table 1**  
Summary of the Observed Objects

Name	$z^a$	$\Delta V_{\text{FWHMcorr}}^b$ (km s $^{-1}$ )	$\lambda_1^c$ (Å)	$\lambda_2^d$ (Å)	$\lambda_3^e$ (Å)	$NB_{\text{auto}}$	$NB_{\text{ap}}^f$	$BV_{\text{ap}}^f$
LAE J221650.2+002750	3.099	171.1	4984.9	0.0	4984.9	25.24	25.68	26.88
LAE J221650.9+002327	3.087	191.1	4970.8	0.0	4970.8	25.00	25.14	26.31
LAE J221652.7+002423	3.067	217.3	4944.7	0.0	4944.7	24.73	24.89	25.89
LAE J221653.9+002137	3.081	402.5	4964.6	4950.9	4966.6	24.57	24.67	26.27
LAE J221658.4+002430	3.102	392.0	4987.1	0.0	4987.1	24.07	24.61	25.90
LAE J221659.3+002304	3.069	306.0	4947.2	0.0	4947.2	23.95	24.92	25.69
LAE J221659.3+002501	3.088	141.5	4970.7	4960.9	4969.3	24.30	24.97	26.08
LAE J221700.3+002404	3.098	96.7	4981.8	0.0	4981.8	24.61	24.78	26.35
LAE J221700.7+002006	3.075	42.5	4955.3	0.0	4956.4	25.17	25.22	26.66
LAE J221701.6+002135	3.070	265.8	4947.6	4932.9	4942.2	24.59	24.96	25.63
LAE J221701.8+002003	3.077	161.9	4956.1	4947.0	4953.1	25.21	25.25	28.03
LAE J221702.7+002433	3.067	385.4	4944.7	0.0	4944.7	23.58	23.88	24.91
LAE J221702.8+002121	3.091	0.0	4973.5	4968.7	4971.7	25.27	25.34	27.70
LAE J221704.9+002226	3.108	279.8	4995.5	0.0	4995.5	24.80	25.26	26.63
LAE J221706.7+002134	3.067	330.4	4944.2	4935.8	4941.9	23.60	24.11	24.97
LAE J221709.6+001801	3.105	924.1	4994.2	0.0	4987.8	23.07	23.08	24.75
LAE J221713.3+002034	3.101	278.0	4987.2	0.0	4987.2	24.73	25.06	27.55
LAE J221713.6+000640	3.113	302.7	5002.0	4991.5	5000.9	23.23	23.31	24.82
LAE J221713.7+001656	3.057	249.4	4934.2	0.0	4934.2	24.75	25.13	26.45
LAE J221715.7+001906	3.101	233.2	4986.7	4972.3	4986.0	24.55	24.60	27.03
LAE J221715.8+002431	3.106	276.5	4992.4	0.0	4992.4	24.47	24.68	26.40
LAE J221716.7+002309	3.066	388.7	4945.7	0.0	4945.7	24.53	25.36	26.61
LAE J221717.3+000728	3.090	149.3	4972.9	0.0	4972.9	24.47	25.18	26.53
LAE J221717.5+002010	3.075	563.1	4954.4	0.0	4954.7	24.65	25.36	28.47
LAE J221718.8+001518	3.067	91.1	4944.8	0.0	4943.4	24.44	24.90	26.98
LAE J221719.0+001200	3.090	265.7	4972.1	4965.6	4970.3	25.03	25.13	26.64
LAE J221719.3+001450	3.065	288.8	4942.8	4935.2	4943.8	24.40	0.00	0.00
LAE J221719.7+001149	3.067	150.1	4945.4	4938.1	4943.4	24.83	0.00	0.00
LAE J221720.1+002226	3.104	226.7	4991.1	0.0	4991.1	24.87	25.40	26.73
LAE J221720.2+002019	3.108	1997.2	5005.8	0.0	4995.0	22.44	22.40	23.43
LAE J221720.3+002438	3.070	201.4	4948.0	4935.9	4943.9	23.59	23.87	25.18
LAE J221721.7+001223	3.068	355.1	4947.0	0.0	4947.0	25.06	25.32	26.90
LAE J221722.3+000804	3.085	88.4	4967.3	4957.4	4962.0	23.81	24.07	25.55
LAE J221722.6+002145	3.104	88.1	4988.4	4978.1	4989.0	25.00	25.05	27.06
LAE J221722.9+001441	3.054	0.0	4929.2	4924.1	4928.7	24.99	25.08	26.90
LAE J221723.5+002040	3.071	368.3	4950.8	4935.7	4950.9	24.76	24.88	26.51
LAE J221723.8+002155	3.102	0.0	4987.2	0.0	4987.2	24.71	25.49	27.09
LAE J221724.6+001557	3.079	172.0	4960.1	4953.5	4958.8	25.34	25.42	28.47
LAE J221724.7+002227	3.091	349.8	4974.4	0.0	4975.2	25.12	25.37	26.75
LAE J221724.8+001717	3.096	358.3	4981.2	0.0	4980.8	23.62	0.00	0.00
LAE J221727.2+001622	3.096	339.5	4978.1	0.0	4978.1	24.67	24.81	26.33
LAE J221727.3+001046	3.069	307.2	4946.9	4938.1	4945.3	24.64	24.77	27.02
LAE J221727.8+001737	3.092	172.9	4975.6	4967.6	4973.2	24.31	24.40	26.97
LAE J221728.3+001212	3.067	162.3	4945.3	0.0	4947.5	24.31	24.51	26.27
LAE J221733.9+001215	3.106	0.0	4991.5	4982.5	4990.7	24.67	25.04	26.93
LAE J221735.9+001559	3.094	673.8	4978.0	0.0	4978.0	24.08	24.68	26.92
LAE J221736.4+001251	3.058	150.5	4934.1	0.0	4934.1	25.20	25.17	27.31
LAE J221736.8+002614	3.069	179.5	4948.0	4942.2	4947.3	24.98	25.06	27.40
LAE J221738.5+002215	3.096	144.4	4980.3	0.0	4980.3	24.85	24.96	26.74
LAE J221738.9+001102	3.064	116.9	4940.9	4929.9	4937.3	23.56	24.06	25.36
LAE J221739.0+001726	3.072	165.0	4951.5	4943.3	4949.0	24.66	0.00	0.00
LAE J221739.2+002242	3.098	189.3	4981.4	0.0	4983.8	25.25	25.52	27.64
LAE J221739.3+001610	3.093	66.0	4976.5	0.0	4976.4	24.84	25.40	27.51
LAE J221739.9+002142	3.089	361.1	4972.8	0.0	4972.8	25.24	25.21	27.66
LAE J221740.3+001129	3.065	71.9	4941.4	0.0	4943.2	25.01	24.58	25.43
LAE J221740.9+001125	3.089	288.4	4968.8	0.0	4968.8	23.49	24.53	25.31
LAE J221741.4+002227	3.096	208.0	4980.9	0.0	4980.9	24.31	24.55	25.35
LAE J221743.3+002149	3.097	88.2	4981.9	4967.8	4975.4	24.68	0.00	0.00
LAE J221743.4+001348	3.098	142.8	4982.1	4975.9	4980.9	23.95	24.01	25.97
LAE J221743.7+002451	3.101	350.0	4987.4	4977.5	4984.3	25.04	25.18	26.91
LAE J221745.3+002006	3.074	195.8	4953.0	4943.9	4950.3	24.00	24.13	26.53
LAE J221745.6+001544	3.065	241.6	4942.3	4933.6	4939.4	24.58	24.59	26.25
LAE J221745.9+002319	3.098	142.8	4981.9	4976.0	4979.9	24.81	0.00	0.00
LAE J221748.6+001334	3.056	93.5	4932.7	4924.5	4930.5	23.90	0.00	0.00
LAE J221750.5+001310	3.089	57.0	4970.6	4965.9	4967.5	25.52	25.35	27.81



**Table 1**  
(Continued)

Name	$z^a$	$\Delta V_{\text{FWHMcorr}}^b$ (km s $^{-1}$ )	$\lambda_1^c$ (Å)	$\lambda_2^d$ (Å)	$\lambda_3^e$ (Å)	$NB_{\text{auto}}$	$NB_{\text{ap}}^f$	$BV_{\text{ap}}^f$
LAE J221751.0+001858	3.081	346.1	4963.7	4954.0	4961.6	24.17	24.42	27.00
LAE J221753.2+001238	3.095	112.4	4977.9	4969.3	4975.1	24.60	0.00	0.00
LAE J221754.3+001224	3.093	184.0	4976.4	0.0	4973.9	24.49	24.50	26.00
LAE J221755.1+002460	3.058	402.7	4935.7	4923.4	4932.3	23.73	24.03	25.33
LAE J221757.6+001204	3.093	282.1	4976.6	4966.1	4973.9	24.38	24.80	26.15
LAE J221759.2+002254	3.087	333.3	4968.2	4958.8	4965.1	23.00	23.34	25.43
LAE J221759.3+001148	3.055	19.4	4928.9	0.0	4929.0	25.41	25.01	25.86
LAE J221802.2+002556	3.081	0.0	4961.5	0.0	4960.3	23.03	23.88	25.97
LAE J221803.6+002247	3.079	133.8	4958.9	0.0	4958.9	25.44	25.42	27.50
LAE J221805.9+002407	3.095	0.0	4979.0	4973.7	4977.0	25.24	25.38	27.25
LAE J221807.9+002317	3.088	131.8	4970.1	4955.8	4964.9	23.97	24.58	26.12
LAE J221808.0+001151	3.096	159.7	4980.1	0.0	4980.1	24.82	25.19	26.33
LAE J221808.3+001022	3.097	421.7	4982.6	4969.6	4980.0	23.02	23.47	24.72
LAE J221809.2+001242	3.096	60.0	4980.1	4972.2	4976.9	24.82	25.05	27.06
LAE J221809.4+001358	3.105	124.5	4989.9	0.0	4989.9	24.96	25.49	26.77
LAE J221811.0+002508	3.095	294.8	4978.9	0.0	4978.9	25.04	25.07	26.59
LAE J221812.5+001433	3.095	164.1	4978.8	0.0	4983.9	23.57	24.15	25.25
LAE J221813.2+002157	3.115	176.1	5003.6	4990.3	4999.2	25.22	25.32	26.37
LAE J221813.8+000925	3.104	110.3	4989.8	4983.0	4987.9	24.83	24.83	27.93
LAE J221813.9+002222	3.089	0.0	4971.3	0.0	4971.3	24.69	0.00	0.00
LAE J221816.0+001412	3.086	74.2	4968.0	4957.4	4964.7	24.24	24.66	26.64
LAE J221817.3+001209	3.087	330.9	4970.8	0.0	4966.6	24.45	24.78	25.77
LAE J221818.2+001143	3.091	315.8	4975.6	0.0	4975.6	25.00	25.17	26.11
LAE J221820.8+001257	3.109	119.2	4996.0	4986.8	4991.7	25.40	25.28	27.52
LAE J221820.8+001241	3.103	342.0	4989.6	4978.0	4986.0	23.78	24.60	26.46
LAE J221820.9+001031	3.097	178.3	4981.3	0.0	4981.3	24.99	25.50	28.16

**Notes.**<sup>a</sup> Redshift measured by the peak of the strongest emission-line component.<sup>b</sup> FWHM of the strongest component after corrected for the instrumental profile. The zero value means that the line is not resolved.<sup>c</sup> The central wavelength of the red peak in the multiple-component Gaussian fitting.<sup>d</sup> The central wavelength of the blue peak in the multiple-component Gaussian fitting.<sup>e</sup> The central wavelength of peak in the single-component Gaussian fitting.<sup>f</sup> The aperture magnitude values are measured in the 2 arcsec diameter apertures.**Table 2**  
Number of LAEs with Characteristic Profile

	All	$NB_{497} < 25$	$NB_{497} < 25, BV - NB > 1.0$
Total	89	53	47
“Red+Blue” profile	39	28	26

In this case, the star formation in these Ly $\alpha$  emitters must be dominated by burst-like events since continuous gas infall is needed to maintain continuous star formation activities. The population of the Ly $\alpha$  emitters is generally considered to be less massive objects in the stellar mass as many of them are not detected even in the deepest ground-based near-infrared images. The early active starburst events may result in galactic wind activity producing the expanding shells. It is important to note that the Ly $\alpha$  emission from  $\sim 44\%$ , and possibly a larger fraction of the observed sample, shows such evidence.

To prove the expanding shell or gas outflow models, another important observational constraint is the surface brightness distribution of the Ly $\alpha$  emission. Rauch et al. (2008) obtained two-dimensional spectra of Ly $\alpha$  emitters and found the surface brightness to be most strongly peaked in the spatial direction, even though the emission could be traced out to several arcseconds. Barnes & Haehnelt (2010) argued that this rapid drop of surface brightness with radius is inconsistent with the much flatter radial profile predicted by a simple expanding shell

model. In fact, there is a weak trend, though not very significant, that the objects with the characteristic profile are rather small (see Section 4.3 and Figures 8 and 9 below). This goes against the interpretation of the simple expanding shell models. On the other hand, for many of the extended objects, such as Ly $\alpha$  blobs, Mori & Umemura (2006) successfully reproduced the observed Ly $\alpha$  morphology by the model of expanding gas heated by supernovae. Future improvements both in observations and models (e.g., Barnes et al. 2011) will allow a more detailed study on the surface brightness distributions.

**4.2. Ly $\alpha$  Blobs**

It is also interesting to discuss the relation between the characteristic line profile and the Ly $\alpha$  blobs. Matsuda et al. (2006) found that the galaxies with a larger size tend to have more structures in the line profiles and a larger “total line width” than FWHM  $\sim 500$  km s $^{-1}$  if fitted by a single Gaussian profile (as in Figure 2(b) or 3(b) in this paper).

For the velocity width, a similar trend is confirmed with the current sample. In Table 3, we listed the velocity FWHM obtained by the single Gaussian fitting, namely, the same procedure as in Matsuda et al. (2006), for the 12 objects associated with the Ly $\alpha$  blobs in Matsuda et al. (2004). Of the 12 objects, 9 have FWHM  $> 450$  km s $^{-1}$ . While the other three objects have a smaller velocity width, LAB32 and LAB33 are among the smallest in the sample of the 35 Ly $\alpha$  blobs in Matsuda

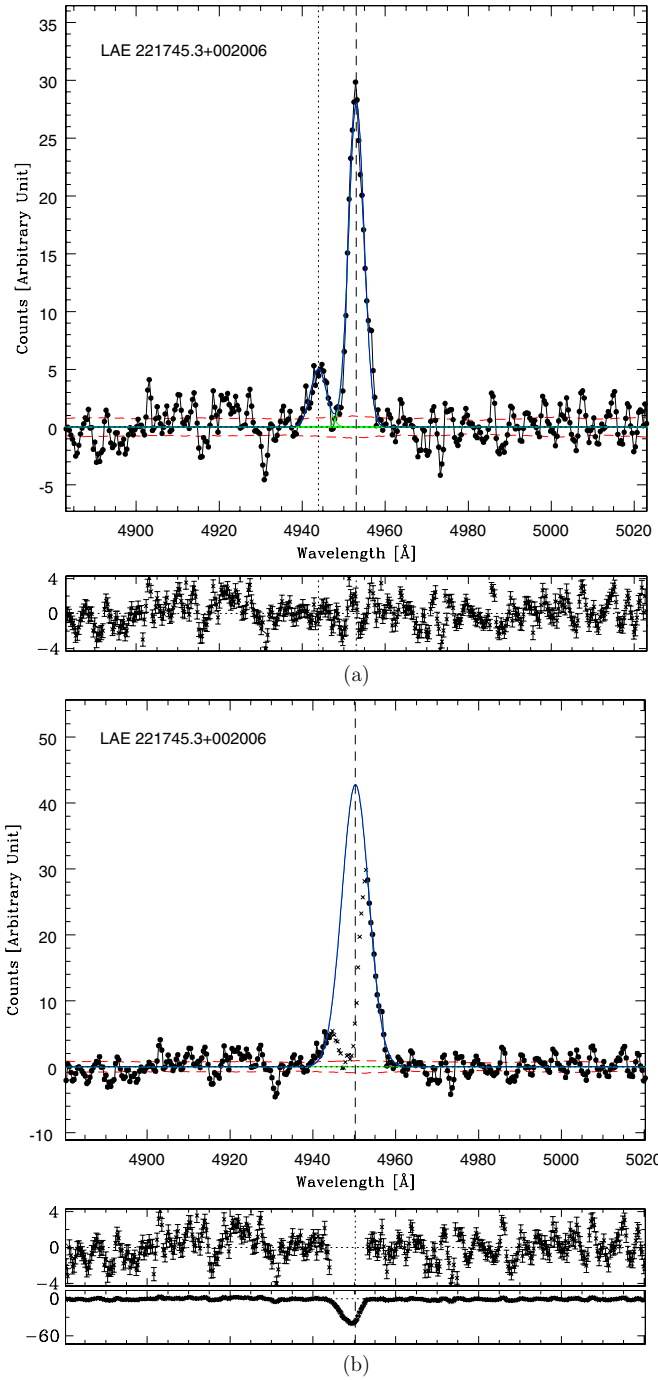


**Figure 2.** (a) Example of the formal multiple Gaussian fitting to the profile of an object observed with the high signal-to-noise ratio. The blue line is the best-fitted Gaussian profiles and the red dashed lines show the background noise level (root-mean-square values). (b) Same as Figure 2(a) but for the formal single Gaussian fitting. The data points used in the fitting are plotted by the filled dots. Crosses are those not used in the fitting. The bottom panels show the formal residuals.

et al. (2004). LAB7 has three or possibly four distinguished Ly $\alpha$  peaks (Matsuda et al. 2004) and the slit position in this study just covers the single southmost peak. The value measured in this observation may not represent the whole nature of the system.

Of the 12 objects associated with the Ly $\alpha$  blobs, only 5 are classified as “strong red and weak blue” profile objects. At a glance, this appears somewhat strange, since the line

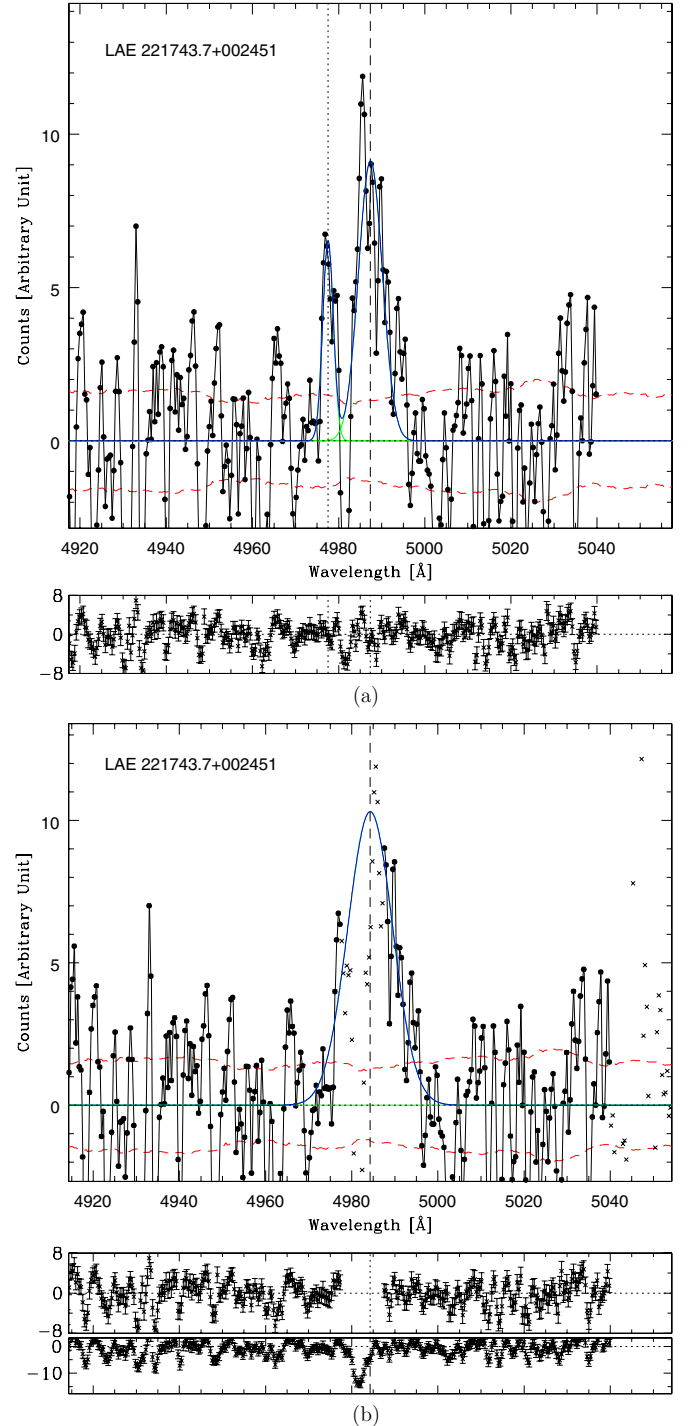


**Figure 3.** (a) Same as Figure 2(a) but for an object with a relatively poor S/N ratio. (b) Same as Figure 2(b) but for an object with a relatively poor S/N ratio.

profiles of the Ly $\alpha$  blobs shown in Matsuda et al. (2006) have more structures with possible absorption than the other smaller emitters. If we look closely at Figure 1, however, there are hints of multiple components that are not significantly detected in the current data. Although it is difficult to conclude, as the exposure time (7 hr in Matsuda et al. 2006), the spectral resolution ( $R \sim 2500$ ), and the instrument (Keck DEIMOS) are different from those in this paper, deeper data may probe significant structures of these lines. Another possible interpretation is as follows. If Ly $\alpha$  blobs are more massive objects, they may have thicker absorbing material and the weak blue line is

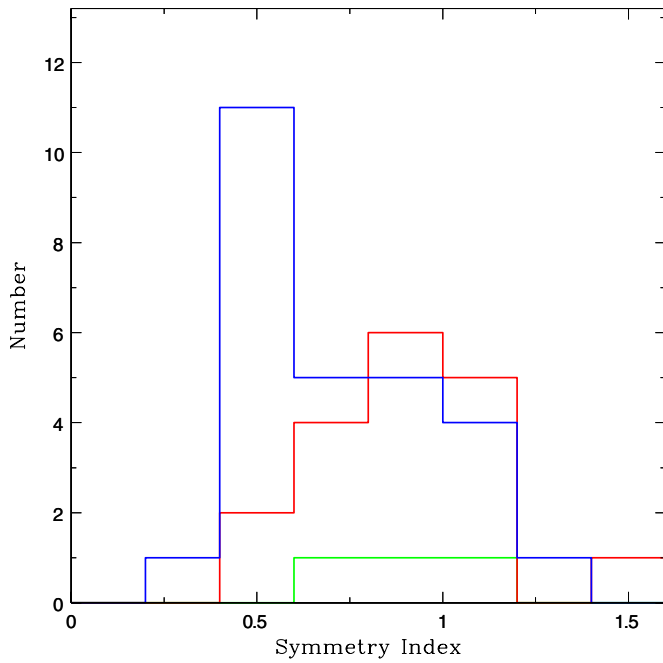


**Figure 4.** Distribution of the symmetry index of the strongest peak in the  $\text{Ly}\alpha$  profile. The objects with the characteristic profile with strong red and weak blue components are shown by the blue histogram, which strongly peaked at 0.5. The objects with strong blue and weak red peaks are shown by the green line. Other objects are shown by the red line.

**Table 3**  
Objects Associated With  $\text{Ly}\alpha$  Blobs

Name	FWHM (Single Gaussian) ( $\text{km s}^{-1}$ )	$\text{Ly}\alpha$ Blobs <sup>a</sup>	Profile <sup>b</sup>
LAE J221658.4+002430	428.8	LAB34	No
LAE J221706.7+002134	562.9	LAB27	Yes
LAE J221723.8+002155	474.3	LAB32	No
LAE J221724.8+001717	474.4	LAB35	No
LAE J221735.9+001559	696.0	LAB14	No
LAE J221738.9+001102	641.2	LAB31	Yes
LAE J221740.9+001125	338.1	LAB7	No
LAE J221759.2+002254	625.5	LAB28	Yes
LAE J221807.9+002317	582.4	LAB23	Yes
LAE J221808.3+001022	738.8	LAB15	Yes
LAE J221812.5+001433	222.1	LAB33	No
LAE J221817.3+001209	661.5	LAB21	No

**Notes.**

<sup>a</sup> Name of the associated  $\text{Ly}\alpha$  blobs listed in Matsuda et al. (2004).

<sup>b</sup> The column indicates whether the  $\text{Ly}\alpha$  line profile shows the characteristic “strong red and weak blue” one (“Yes”) or not (“No”).

too absorbed to be detected. This is likely to be the case for those with the single but asymmetrical component, such as LAE J221808.3+001022 (LAB15), LAE J221812.5+001433 (LAB33), and LAE J221817.3+001209 (LAB21).

Matsuda et al. (2006) argued that the large velocity width implies that  $\text{Ly}\alpha$  blobs are objects more massive than other “normal”  $\text{Ly}\alpha$  emitters. The large size of the  $\text{Ly}\alpha$  emission of the blobs can be explained by either the expanding gas ionized and excited by the supernova feedback (Mori & Umemura 2006) or by the infalling cooling gas (Haiman et al. 2000; Fardal et al. 2001). While recent models of the cold flows can also reproduce the size and luminosity distribution of the  $\text{Ly}\alpha$  blobs (Dekel et al. 2009; Goerdt et al. 2010), the gas outflow interpretation may be

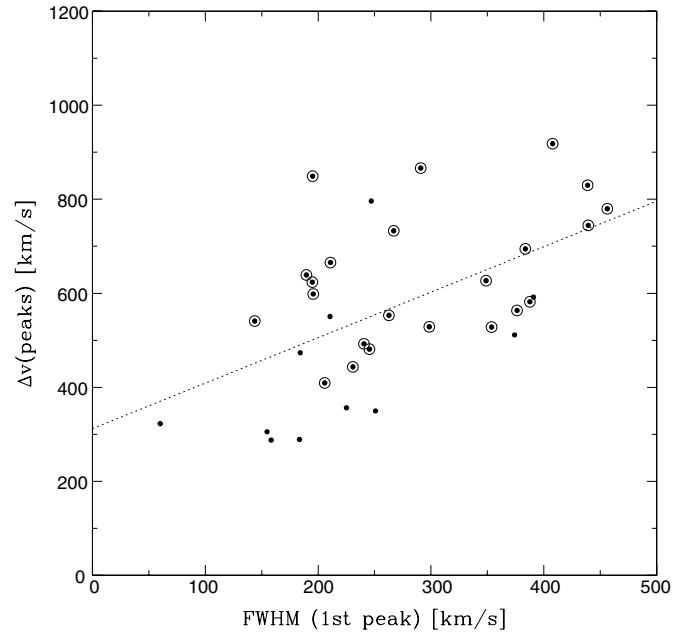


**Figure 5.** Correlation between the observed width of the strongest peak and the separation of the first and the second peaks for the multiple peak objects. Those with relatively good S/N, with  $NB497 < 25$  and  $BV - NB497 > 1.0$  are marked by the large open circles. The dotted line is the best-fit regression line.

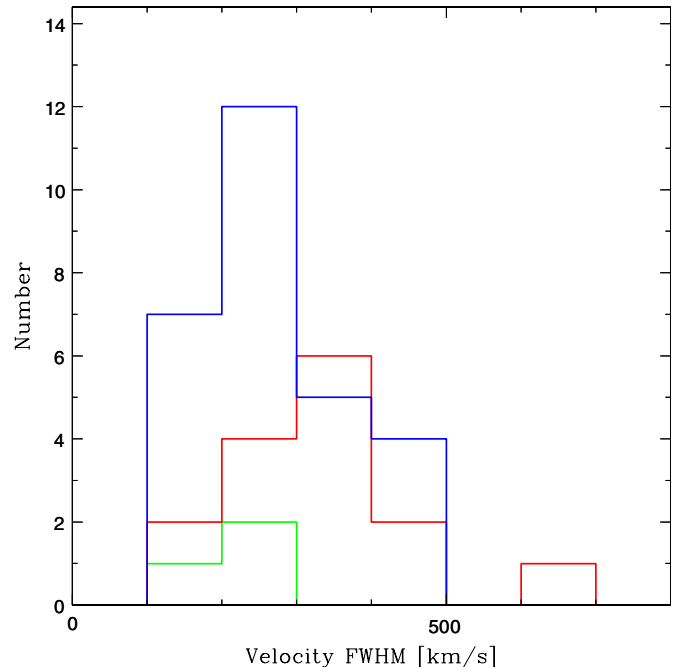


**Figure 6.** Observed velocity FWHM before the instrumental correction for the most prominent peak of each object. Those with relatively good S/N, with  $NB497 < 25$  and  $BV - NB497 > 1.0$ , are used. Same as in Figure 4, the blue and red lines show the objects with multiple characteristic peaks and those with a single peak, respectively.

favorable if the  $\text{Ly}\alpha$  blobs are the scaled-up version of normal emitters whose line profiles are dominated by the outflowing gas.

#### 4.3. Correlation with Other Properties

We also investigated whether the presence of the characteristic profile is related to any other properties of  $\text{Ly}\alpha$  emitters. First, we see the distribution of the observed excess in

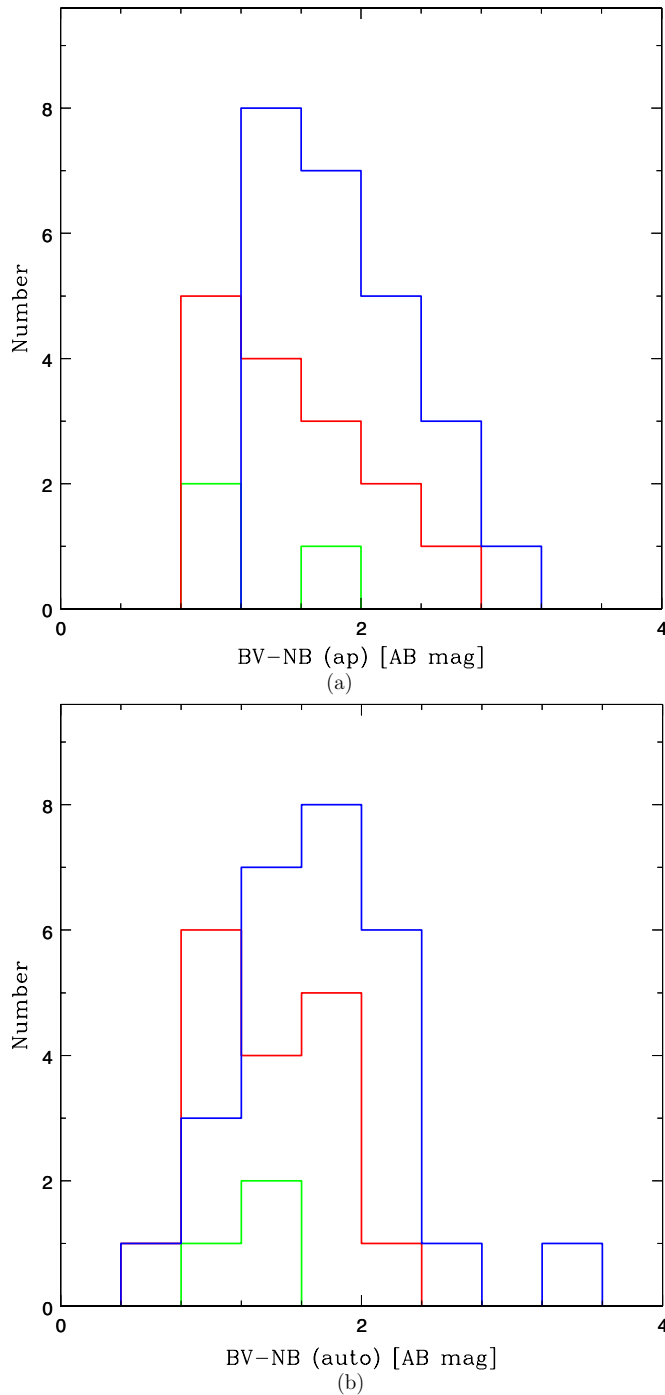


**Figure 7.** (a) The distribution of  $BV - NB497$  color, namely, the observed excess in the narrow band. Panel (a) shows the values measured in 2 arcsec diameter aperture while panel (b) shows those for the MAG\_AUTO semi-total magnitude. The lines have the same meaning as in Figure 6.

$BV - NB497$  color, or an equivalent width, in Figures 7(a) and (b). Figure 7(a) shows the result for the color measured in the fixed 2'' diameter aperture and Figure 7(b) shows those for the semi-total flux measured in the Kron aperture (i.e., SExtractor MAG\_AUTO) for those LAEs with  $NB497 < 25.0$  mag. The emitters with the characteristic profile seem to dominate at the range  $BV - NB497 > 1.8$ , where 13 of the 16 objects show “strong red and weak blue” peaks. On the other hand, the  $BV - NB497$  color excess of the objects with the characteristic profile is not always large. The trend is also notable in

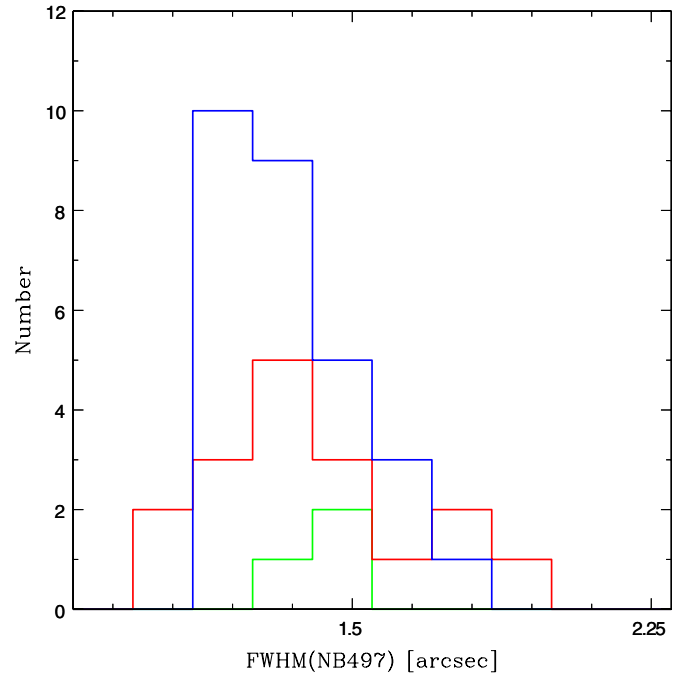


**Figure 8.** Distribution of the size of the  $\text{Ly}\alpha$  emitters in FWHM in their surface brightness profile. The lines have the same meaning as in Figure 6.

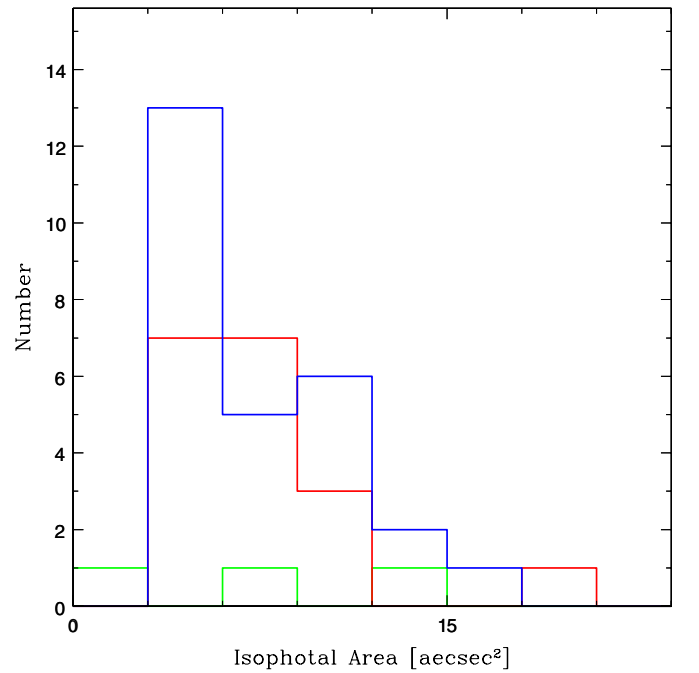


**Figure 9.** Distribution of the narrowband isophotal area above the detection threshold. The lines have the same meaning as in Figure 6.

Figure 7(b). The probabilities from the Kolmogorov–Smirnov test that follow the same distribution are 17% and 9%, respectively. The large excess in the narrow band or  $\text{Ly}\alpha$  equivalent width can be related to the gas outflow, such as additional  $\text{Ly}\alpha$  emission, due to the collisional excitation or ionization by the shock. If the source of the  $\text{Ly}\alpha$  emission is photoionization by massive stars, the large equivalent width suggests the presence of a very young or metal-poor stellar population, which is also consistent with the gas outflow by the supernovae or strong stellar wind.

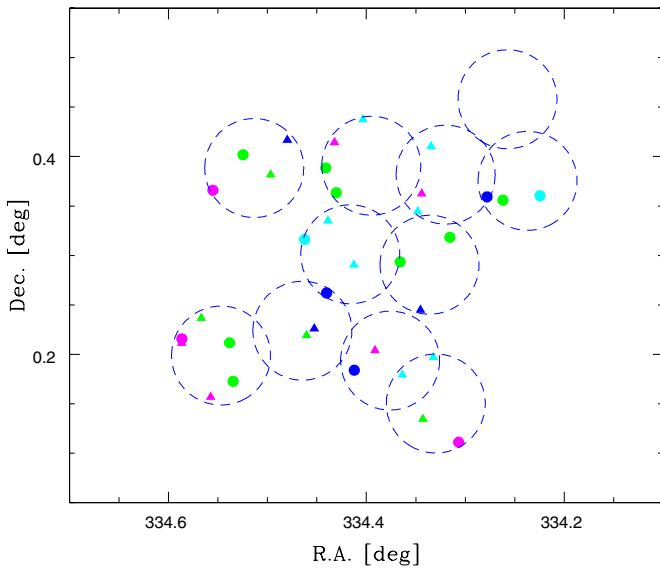


**Figure 10.** Sky distribution of the objects with the characteristic profiles. The dashed large circle shows the FOCAS slit mask areas. The objects with different symbols and colors have a different redshift for the absorption in the formal Gaussian fitting. Redshift increases from 3.047 to 3.129 in intervals of 0.008, in order of blue (circle), cyan (triangle), green, magenta, and red colors.

We also studied the distributions of the size, the observed FWHM, and the isophotal area above the detection threshold, and the results are shown in Figures 8 and 9. To omit the objects with a low S/N ratio, we again limited the sample to those with  $NB497 < 25.0$  and  $BV - NB497 > 1.0$ . While the distributions for the objects with and without the characteristic profile are not quite distinguishable, there is some concentration of the “strong red and weak blue” object for smaller sizes (Kolmogorov–Smirnov test probability is 15%). This is disadvantageous for the simple expanding shell model, which predicts a rather flat surface brightness distribution. If the starburst is so young, however, the area of the outflowing gas can be still very limited within the small radius from the galactic center to show nearly unresolved morphology.

#### 4.4. Intergalactic Absorption in Protocluster?

Finally, we revisit the possibility that the characteristic profile is caused by the intergalactic absorption systems. As the field is known to have a high density of star-forming galaxies (Steidel et al. 1998, 2000; Hayashino et al. 2004), the neutral gas density may also be enhanced along the filamentary large-scale structure. The characteristic profile can be caused by the absorption of the common gas in such a structure in front of the observed emitters. In such a case, absorption redshift is expected to be spatially correlated. Figure 10 shows the sky distribution of the  $\text{Ly}\alpha$  emitters with the characteristic profile. The redshift

of the “absorption” that was formally obtained by the single-component Gaussian fitting allowing the absorption features are color-coded, from redshift 3.047 to 3.129 in intervals of 0.008 ( $600 \text{ km s}^{-1}$ ). No large-scale correlation of the absorption redshift is seen.

We thank the staff of the Subaru Telescope for their assistance. This research is supported in part by the Grant-in-Aid 20450224 for Scientific Research of the Ministry of Education, Science, Culture, and Sports in Japan. Data analysis was in part carried out on the common use data analysis computer system at the Astronomy Data Center, ADC, of the National Astronomical Observatory of Japan.

#### REFERENCES

- Barnes, L. A., & Haehnelt, M. G. 2010, *MNRAS*, **403**, 870  
 Barnes, L. A., Haehnelt, M. G., Tescari, E., & Viel, M. 2011, *MNRAS*, **416**, 1723  
 Dekel, A., Birnboim, Y., Engel, G., et al. 2009, *Nature*, **457**, 451  
 Dijkstra, M., Haiman, Z., & Spaans, M. 2006a, *ApJ*, **649**, 14  
 Dijkstra, M., Haiman, Z., & Spaans, M. 2006b, *ApJ*, **649**, 37  
 Dijkstra, M., Lidz, A., & Wyithe, J. S. B. 2007, *MNRAS*, **377**, 1175  
 Fardal, M. A., Katz, N., Gardner, J. P., et al. 2001, *ApJ*, **562**, 605  
 Finkelstein, S. L., Rhoads, J. E., Malhotra, S., Pirzkal, N., & Wang, J. 2007, *ApJ*, **660**, 1023  
 Gawiser, E., Francke, H., Lai, K., et al. 2007, *ApJ*, **671**, 278  
 Goerdt, T., Dekel, A., Sternberg, A., et al. 2010, *MNRAS*, **407**, 613  
 Gronwall, C., Ciardullo, R., Hickey, T., et al. 2007, *ApJ*, **667**, 79  
 Haiman, Z., Spaans, M., & Quataert, E. 2000, *ApJ*, **537**, L5  
 Hayashino, T., Matsuda, Y., Tamura, H., et al. 2004, *AJ*, **128**, 2073  
 Hayes, M., Östlin, G., Schaerer, D., et al. 2010, *Nature*, **464**, 562  
 Hayes, M., Scarlata, C., & Siana, B. 2011, *Nature*, **476**, 304  
 Hu, E., & McMahon, R. G. 1996, *Nature*, **382**, 281  
 Iye, M., Ota, K., Kashikawa, N., et al. 2006, *Nature*, **443**, 186  
 Kodaira, K., Taniguchi, Y., Kashikawa, N., et al. 2003, *PASJ*, **55**, L17  
 Laursen, P., Sommer-Larsen, J., & Razoumov, A. O. 2011, *ApJ*, **728**, 52  
 Madau, P., & Shull, J. M. 1996, *ApJ*, **457**, 551  
 Matsuda, Y., Yamada, T., Hayashino, T., Yamauchi, R., & Nakamura, Y. 2006, *ApJ*, **640**, L123  
 Matsuda, Y., Yamada, T., Hayashino, T., et al. 2004, *AJ*, **128**, 569  
 Matsuda, Y., Yamada, T., Hayashino, T., et al. 2005, *ApJ*, **634**, L125  
 McLinden, E. M., Finkelstein, S. L., Rhoads, J. E., et al. 2011, *ApJ*, **730**, 136  
 Mori, M., & Umemura, M. 2006, *Nature*, **440**, 644  
 Ouchi, M., Shimasaku, K., Akiyama, M., et al. 2008, *ApJS*, **176**, 301  
 Palunas, P., Teplitz, H. I., Francis, P. J., Williger, G. M., & Woodgate, B. E. 2004, *ApJ*, **602**, 545  
 Pettini, M., Shapley, A. E., Steidel, C. C., et al. 2001, *ApJ*, **554**, 981  
 Rauch, M., Haehnelt, M., Bunker, A., et al. 2008, *ApJ*, **681**, 856  
 Rhoads, J. E., Dey, A., Malhotra, S., et al. 2003, *AJ*, **125**, 1006  
 Rhoads, J. E., & Malhotra, S. 2001, *ApJ*, **563**, L5  
 Shapley, A. E., Steidel, C. C., Pettini, M., & Adelberger, K. L. 2003, *ApJ*, **588**, 65  
 Steidel, C. C., Adelberger, K. L., Dickinson, M., et al. 1998, *ApJ*, **492**, 428  
 Steidel, C. C., Adelberger, K. L., Shapley, A. E., et al. 2000, *ApJ*, **532**, 170  
 Steidel, C. C., Erb, D. K., Shapley, A. E., et al. 2010, *ApJ*, **717**, 289  
 Taniguchi, Y., Ajiki, M., Nagao, T., et al. 2005, *PASJ*, **57**, 165  
 Verhamme, A., Schaerer, D., Atek, H., & Tapken, C. 2008, *A&A*, **491**, 89  
 Verhamme, A., Schaerer, D., & Maselli, A. 2006, *A&A*, **460**, 397  
 Yamada, T., Nakamura, Y., Matsuda, Y., et al. 2012, *AJ*, **143**, 79